Stationary-Frame Complex-Valued Frequency-Domain Modeling of Three-Phase Power Converters

Liao, Yicheng; Wang, Xiongfei

Published in:
IEEE Journal of Emerging and Selected Topics in Power Electronics

DOI (link to publication from Publisher):
10.1109/JESTPE.2019.2958938

Publication date:
2020

Document Version
Publisher's PDF, also known as Version of record

Stationary-Frame Complex-Valued Frequency-Domain Modeling of Three-Phase Power Converters

Yicheng Liao, *Student Member, IEEE*, and Xiongfei Wang, *Senior Member, IEEE*

***Abstract*— The stationary-frame complex-valued frequency-domain modeling has been applied to characterize the frequency-coupling dynamics of three-phase converters. Yet, those models are generally derived through mathematical transformations of the linearized time-invariant models in the rotating *dq*-frame. A step-by-step modeling method with clear physical insight in the stationary frame is still missing. This article attempts to fill in the void by introducing a general stationary ($\alpha\beta$)-frame, three-port equivalent circuit model for the converter power stage, based on the direct linearization around time-periodic trajectories. The model not only reveals the frequency-coupling effect of the ac–dc dynamic interaction but also provides an explicit theoretical basis for incorporating the control dynamics. Moreover, the dependence of the frequency-coupling terms on the initial phase of the input voltage is pointed out. Considering the phase-dependent feature, a frequency scan method that can accurately measure the $\alpha\beta$-frame converter model is proposed. The measured frequency responses in both the nonlinear time-domain simulations and experimental tests validate the effectiveness of the frequency scan method and the theoretical analysis.**

***Index Terms*— Complex vector, frequency coupling, impedance measurement, phase dependence, stationary($\alpha\beta$)-frame model, voltage-source converter (VSC).**

I. Introduction

THE frequency-domain modeling and analysis is an efficient approach for dynamic studies of electric power systems [1]. The converter-based power systems feature highly nonlinear and wide timescale dynamics, which make the modeling and analysis significantly different from the legacy power systems that are dominated by synchronous generators [2].

Over the past decades, the frequency-domain modeling of three-phase power converters has drawn increasing attention. In earlier applications, the line-commutated converters (LCCs) were deployed in high-voltage dc systems. It was reported that the LCC can be linearized as a time-periodic system, which features the frequency-coupling and phase-dependent dynamics [3]. The frequency coupling indicates the dynamic coupling between different frequency components caused by the time-periodic operating trajectory, and the phase dependence implies the dependence of the frequency-coupling dynamics on the initial phase of the time-periodic trajectory. These impacts in the LCCs were mainly studied at specific harmonics [4]–[7]. In recent years, the voltage-source converters (VSCs) have been widely used in modern power systems. Differing from LCCs, VSCs provide a full controllability over the power and current, whose multi-timescale control dynamics tend to result in instability phenomena across a wide frequency range [8]. Consequently, the frequency-domain modeling of VSCs becomes important for the stability analysis and control of modern power-electronic-based systems.

Similar to the LCC, the VSC also behaves as a time-periodic system, which intrinsically features the frequency-coupling and phase-dependent properties. The classical way to model the VSC is to utilize the Park transformation to transform the time-periodic operating trajectory as the time-invariant operating point in the synchronous (*dq*)-frame, and then linearize the system as a linear time-invariant (LTI) multi-input multi-output (MIMO) system based on real vectors [9]–[11]. However, this *dq*-frame real-valued model hides the frequency couplings and phase dependence, since the reference frame is synchronized with the steady-state operating trajectory. Alternatively, the *dq*-frame modeling can be extended to the complex space based on complex vectors through mathematical transformations [1], [12], which is called as *dq*-frame complex-valued model hereafter and also known as the modified sequence-domain model in [13] and [14]. Such a model points out the frequency-coupling and phase-dependent behaviors of asymmetrically-controlled VSCs [13], yet it is still represented in the *dq*-frame. The phase-dependent behavior is related to the dynamic phase of the input voltage, which usually requires a phase-locked loop (PLL) to detect the *dq*-frame responses [15]. Consequently, the dynamic of the PLL tends to affect the validation of the model [16].

To avoid using Park transformations, VSCs can be modeled directly in the $\alpha\beta$-frame [2], [17]–[20]. There are three modeling methods reported, i.e., the harmonic state-space (HSS) modeling [17], [18], the harmonic linearization [19], and the $\alpha\beta$-frame complex-valued impedance model [20]. The general principle of these methods is to linearize the VSC directly around their time-periodic operating trajectories [17], instead of the time-invariant operating points in the *dq*-frame. Thus, a linear time-periodic (LTP) model can be obtained, which can, then, be transformed into the frequency domain and further be represented by harmonic transfer functions [21].

Manuscript received May 10, 2019; revised August 20, 2019 and October 27, 2019; accepted December 5, 2019. Date of publication December 23, 2019; date of current version May 6, 2020. Recommended for publication by Associate Editor Oskar Wallmark. *(Corresponding author: Xiongfei Wang.)*

The authors are with the Department of Energy Technology, Aalborg University, 9220 Aalborg, Denmark (e-mail: ycl@et.aau.dk; xwa@et.aau.dk).

Color versions of one or more of the figures in this article are available online at http://ieeexplore.ieee.org.

Digital Object Identifier 10.1109/JESTPE.2019.2958938

Since the HSS model is represented by the Fourier coefficients of the steady-state trajectory, which are based on real vectors, the obtained harmonic transfer function matrix is of high order [2] and consequently complicates the dynamic analysis. The harmonic linearization method was extended in [19] to model the interactions of multiple harmonics in the modular multilevel converters, which also yields a $\alpha\beta$-frame complex-valued model. Yet, there is a lack of an explicit mathematical basis in this multiharmonic linearized model. Later on, a unified impedance model was developed in [20], by which the mathematical relationship between the dq-frame model and the $\alpha\beta$-frame complex-valued model was rigorously derived. The unified impedance model also allows reducing the model order in contrast to the HSS model, yet it was merely derived from the dq-frame model through mathematical transformations, while a step-by-step modeling approach with clear physical insight is still missing for the $\alpha\beta$-frame complex-valued model. Moreover, the impact of the phase dependence on the $\alpha\beta$-frame complex-valued model was overlooked in [19] and [20], which leads to challenges to the model validation in the frequency domain. It is noted that such a phase dependence in the $\alpha\beta$-frame model is not related to the dynamic phase of the input voltage like that in the dq-frame model, since the $\alpha\beta$-frame model does not need the Park transformation that is time-and-frequency dependent. A refined frequency scan approach to measuring the $\alpha\beta$-frame complex-valued impedance was recently reported in [22]. The method does consider the phase dependence of the frequency-coupling terms, yet it can only measure the diagonal elements of the impedance matrix, whereas the off-diagonal elements still cannot be verified.

To further explore the modeling and validation solutions for the $\alpha\beta$-frame complex-valued model of VSCs, this article proposes first a general $\alpha\beta$-frame, three-port small-signal circuit model for the converter power stage, based on complex vectors and linearizations directly around the time-periodic trajectories. The three-port equivalent circuit model not only reveals the frequency-coupling and phase-dependent characteristics of the ac–dc power conversion, but also provides an explicit mathematical basis for modeling the closed-loop control dynamics for VSCs. Based on the rigorous derivation, the physical insight behind the $\alpha\beta$-frame complex-valued model is clarified, i.e., the phase dependence is merely related to the initial phase of the input voltage, which appears together with the frequency-coupling terms. Considering the phase dependence, a frequency-scan approach to accurately validating the $\alpha\beta$-frame frequency-domain model is further developed. An important advantage of the validation approach over that reported in [22] is that all the elements of the $\alpha\beta$-frame transfer matrices can be directly measured. The effectiveness of the frequency scan approach and the theoretical findings are finally validated by nonlinear time-domain simulations and experimental tests.

II. Stationary-Frame Frequency-Domain Model

In this section, the complex vectors and their implications in three-phase systems are discussed first, and then a general step-by-step modeling procedure for the stationary ($\alpha\beta$)-frame complex-valued model of VSCs is introduced.

A. Complex-Vector Representations and Their Implications

In a three-phase three-wire system with no zero-sequence component, the three-phase voltage in the $\alpha\beta$-frame can be denoted by a two-dimensional (2-D) vector in the real space, i.e., $[v_\alpha,\ v_\beta]^{\mathrm{T}}$, or a 2-D vector in the complex space, i.e., $[\mathbf{v}, \mathbf{v}^*]^{\mathrm{T}}$, where $\mathbf{v}$ and $\mathbf{v}^*$ are defined as two base vectors for the 2-D complex space

$$\begin{bmatrix} \mathbf{v} \\ \mathbf{v}^* \end{bmatrix} = \begin{bmatrix} v_\alpha + jv_\beta \\ v_\alpha - jv_\beta \end{bmatrix} \leftrightarrow \begin{bmatrix} \mathbf{V}(s) \\ \mathbf{V}^*(s) \end{bmatrix} = \begin{bmatrix} V_\alpha(s) + jV_\beta(s) \\ V_\alpha(s) - jV_\beta(s) \end{bmatrix} \tag{1}$$

where the left-side small letters represent the time-domain signals and the right-side capital letters denote the corresponding frequency-domain signals. Bold letters are used to represent complex vectors. The conjugate operator, i.e., "$*$," maps the conversion between the two base vectors.

The dq-frame complex-valued voltage can be defined in a similar way but with the subscript "dq," which is given as

$$\begin{bmatrix} \mathbf{v}_{dq} \\ \mathbf{v}_{dq}^* \end{bmatrix} = \begin{bmatrix} v_d + jv_q \\ v_d - jv_q \end{bmatrix} \leftrightarrow \begin{bmatrix} \mathbf{V}_{dq}(s) \\ \mathbf{V}_{dq}^*(s) \end{bmatrix} = \begin{bmatrix} V_d(s) + jV_q(s) \\ V_d(s) - jV_q(s) \end{bmatrix}. \tag{2}$$

The Park transformation maps the conversion from the $\alpha\beta$-frame to the dq-frame, which is denoted by an exponential operator in the time domain, i.e., $e^{-j\theta_1}$, where $\theta_1 = \omega_1 t + \varphi_1$, ω_1 denotes the fundamental angular frequency, and φ_1 is the initial phase of the fundamental-frequency voltage. Such an exponential operator represents an angle rotation, which can apply to both signals and systems, yet have different implications.

If the exponential operator applies to a signal, there exists

$$\mathbf{v}_{dq} = e^{-j\theta_1}\mathbf{v} \leftrightarrow \mathbf{V}_{dq}(s) = e^{-j\varphi_1}\mathbf{V}(s + j\omega_1) \tag{3}$$

$$\mathbf{v} = e^{j\theta_1}\mathbf{v}_{dq} \leftrightarrow \mathbf{V}(s) = e^{j\varphi_1}\mathbf{V}_{dq}(s - j\omega_1). \tag{4}$$

It is clear that the angle rotation not only results in a frequency shift but also involves an initial phase rotation. The same relationship also applies to other ac vectors, such as the current vector or the duty-cycle vector [11].

For a system, whose complex-valued transfer function $\mathbf{G}(s)$ is represented by an operator $\mathbf{G}(p)$ in the time domain, where $p = d/dt$ [12], the effects of a pair of angle rotations on the system transfer function can be denoted by the following equations:

$$e^{-j\theta_1}\mathbf{G}(p)e^{j\theta_1} = \mathbf{G}(p + j\omega_1) \leftrightarrow \mathbf{G}(s + j\omega_1) \tag{5}$$

$$e^{j\theta_1}\mathbf{G}(p)e^{-j\theta_1} = \mathbf{G}(p - j\omega_1) \leftrightarrow \mathbf{G}(s - j\omega_1). \tag{6}$$

It is seen that the pair of angle rotations only results in a frequency shift since the initial phase rotations can be canceled.

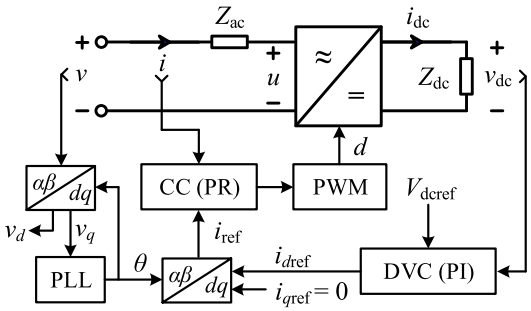

Fig. 1. Single-line diagram of a three-phase VSC with multitimescale control loops.

B. Stationary-Frame Three-Port Circuit Model of Converter Power Stage

Fig. 1 shows a single-line diagram of a three-phase VSC, where the PLL, the current control (CC) loop with a proportional + resonant (PR) regulator, and the dc-link voltage control (DVC) loop with a proportional + integral (PI) regulator are considered in this article.

A three-port small-signal circuit model for the converter power stage shown in Fig. 2 is proposed in this part, which is derived based on the use of $\alpha\beta$-frame complex vectors and the linearization around the steady-state time-periodic trajectory. The detailed derivation is presented as follows.

Similar to the conventional dq-frame small-signal modeling, the state-space averaging operator is applied here to remove the switching ripples [9], and $\mathbf{d} = d_\alpha + jd_\beta$ and $\mathbf{d}^* = d_\alpha - jd_\beta$ are defined as the averaged duty cycle vectors in the $\alpha\beta$-frame. Such complex-vector representations apply to all the ac-side variables shown in Fig. 1. The voltage and current conversions between the ac and dc sides of the VSC can be represented by complex vectors in the $\alpha\beta$-frame as

$$\mathbf{u} = u_\alpha + ju_\beta = d_\alpha v_{dc} + jd_\beta v_{dc} = \mathbf{d}v_{dc} \tag{7}$$

$$\begin{aligned} i_{dc} &= d_\alpha i_\alpha + d_\beta i_\beta = \frac{\mathbf{d}+\mathbf{d}^*}{2}\cdot\frac{\mathbf{i}+\mathbf{i}^*}{2} + \frac{\mathbf{d}-\mathbf{d}^*}{2j}\cdot\frac{\mathbf{i}-\mathbf{i}^*}{2j} \\ &= \frac{1}{2}(\mathbf{d}\mathbf{i}^* + \mathbf{d}^*\mathbf{i}). \end{aligned} \tag{8}$$

Then, combining the ac- and dc-side circuits, there exists

$$\mathbf{v} = Z_{ac}(p)\mathbf{i} + \mathbf{u} = Z_{ac}(p)\mathbf{i} + \mathbf{d}v_{dc} \tag{9a}$$

$$v_{dc} = Z_{dc}(p)i_{dc} = \frac{1}{2}Z_{dc}(p)(\mathbf{d}\mathbf{i}^* + \mathbf{d}^*\mathbf{i}) \tag{9b}$$

which represents the time-domain model of the VSC power stage in the $\alpha\beta$-frame. Differing from the dq-frame model that consists of steady-state operating points, the $\alpha\beta$-frame model is based on steady-state operating trajectories [2]. The linearization is thus done directly around the steady-state operating trajectories, by expanding (9) with steady states plus small perturbations. Then, omitting the steady-state variables, the small-signal model can be derived as

$$\hat{\mathbf{v}} = Z_{ac}(p)\hat{\mathbf{i}} + V_{dc}\hat{\mathbf{d}} + D_{dq}e^{j\theta_1}\hat{v}_{dc} \tag{10a}$$

$$\begin{aligned} \hat{v}_{dc} = \frac{1}{2}Z_{dc}(p)\big(&I_{dq}^* e^{-j\theta_1}\hat{\mathbf{d}} + D_{dq}e^{j\theta_1}\hat{\mathbf{i}}^* \\ &+ D_{dq}^* e^{-j\theta_1}\hat{\mathbf{i}} + I_{dq}e^{j\theta_1}\hat{\mathbf{d}}^*\big) \end{aligned} \tag{10b}$$

where the symbols with "^" denote small perturbations. D_{dq} and I_{dq} are the steady-state complex values in the dq-frame. The exponential operators present in (10) are actually time periodic at the fundamental frequency, which imply the existence of the steady-state trajectories [20]. Here, the exponential operators are intentionally combined with the signals, then it can be seen from (10a) that the ac input $\hat{\mathbf{v}}$ results in the response of $e^{j\theta_1}\hat{v}_{dc}$ at the dc side. Applying the angle rotation, $e^{j\theta_1}$, to (10b) yields

$$\begin{aligned} e^{j\theta_1}\hat{v}_{dc} = \frac{1}{2}&Z_{dc}(p - j\omega_1) \\ &\times \big(I_{dq}^*\hat{\mathbf{d}} + D_{dq}e^{j2\theta_1}\hat{\mathbf{i}}^* + D_{dq}^*\hat{\mathbf{i}} + I_{dq}e^{j2\theta_1}\hat{\mathbf{d}}^*\big) \end{aligned} \tag{11}$$

where besides the responses of $\hat{\mathbf{i}}$ and $\hat{\mathbf{d}}$, the responses of $e^{j2\theta_1}\hat{\mathbf{i}}^*$ and $e^{j2\theta_1}\hat{\mathbf{d}}^*$ are also generated on the ac side.

To derive the general forms of the ac- and dc-side signals, the complex conjugate and the angle rotation of $e^{j2\theta_1}$ are applied to (10a) successively, yielding

$$e^{j2\theta_1}\hat{\mathbf{v}}^* = Z_{ac}(p - j2\omega_1)e^{j2\theta_1}\hat{\mathbf{i}}^* + V_{dc}e^{j2\theta_1}\hat{\mathbf{d}}^* + D_{dq}^* e^{j\theta_1}\hat{v}_{dc}. \tag{12}$$

It is noted that the complex conjugate and the angle rotation are both nonlinear operations, so they are not exchangeable in modeling. Then, from (10a), (11), and (12), it can be derived that

$$\begin{aligned} \begin{bmatrix} \hat{\mathbf{v}} \\ e^{j2\theta_1}\hat{\mathbf{v}}^* \end{bmatrix} = &\begin{bmatrix} Z_{ac}(p) & \\ & Z_{ac}(p - j2\omega_1) \end{bmatrix}\begin{bmatrix} \hat{\mathbf{i}} \\ e^{j2\theta_1}\hat{\mathbf{i}}^* \end{bmatrix} \\ &+ V_{dc}\begin{bmatrix} \hat{\mathbf{d}} \\ e^{j2\theta_1}\hat{\mathbf{d}}^* \end{bmatrix} + \begin{bmatrix} D_{dq} \\ D_{dq}^* \end{bmatrix} e^{j\theta_1}\hat{v}_{dc} \end{aligned} \tag{13a}$$

$$\begin{aligned} e^{j\theta_1}\hat{v}_{dc} = &\frac{1}{2}Z_{dc}(p - j\omega_1)\begin{bmatrix} D_{dq}^* & D_{dq} \end{bmatrix}\begin{bmatrix} \hat{\mathbf{i}} \\ e^{j2\theta_1}\hat{\mathbf{i}}^* \end{bmatrix} \\ &+ \frac{1}{2}Z_{dc}(p - j\omega_1)\begin{bmatrix} I_{dq}^* & I_{dq} \end{bmatrix}\begin{bmatrix} \hat{\mathbf{d}} \\ e^{j2\theta_1}\hat{\mathbf{d}}^* \end{bmatrix}. \end{aligned} \tag{13b}$$

According to (13), the three-port small-signal model of the VSC can be obtained, as shown in Fig. 2. The corresponding open-loop model of the VSC is derived, as shown in Fig. 3, where $\mathbf{v}_{ac}$ and $\mathbf{d}_{ac}$ are input signals, and $\mathbf{i}_{ac}$ and $e^{j\theta_1}v_{dc}$ are output signals. $\mathbf{Z}_{ac}$ is defined as

$$[\mathbf{Z}_{ac}]_{2\times 2} = \begin{bmatrix} Z_{ac}(s) & \\ & Z_{ac}(s - j2\omega_1) \end{bmatrix} \tag{14}$$

where the "$[]_{2\times 2}$" is added here to denote that the matrix $\mathbf{Z}_{ac}$ is a two-by-two matrix, which is omitted in later analysis for brevity. Then the four complex transfer matrices in Fig. 3 can then be derived as

$$[\mathbf{Z}_{ol}]_{2\times 2} = \mathbf{Z}_{ac} + \frac{1}{2}Z_{dc}(s - j\omega_1)\begin{bmatrix} D_{dq}D_{dq}^* & D_{dq}^2 \\ D_{dq}^{*2} & D_{dq}D_{dq}^* \end{bmatrix} \tag{15}$$

$$\begin{aligned} [\mathbf{G}_{di}]_{2\times 2} = -\mathbf{Z}_{ol}^{-1}\Bigg(&V_{dc}\begin{bmatrix} 1 & \\ & 1 \end{bmatrix} + \frac{Z_{dc}(s - j\omega_1)}{2} \\ &\times \begin{bmatrix} D_{dq}I_{dq}^* & D_{dq}I_{dq} \\ D_{dq}^* I_{dq}^* & D_{dq}^* I_{dq} \end{bmatrix}\Bigg) \end{aligned} \tag{16}$$

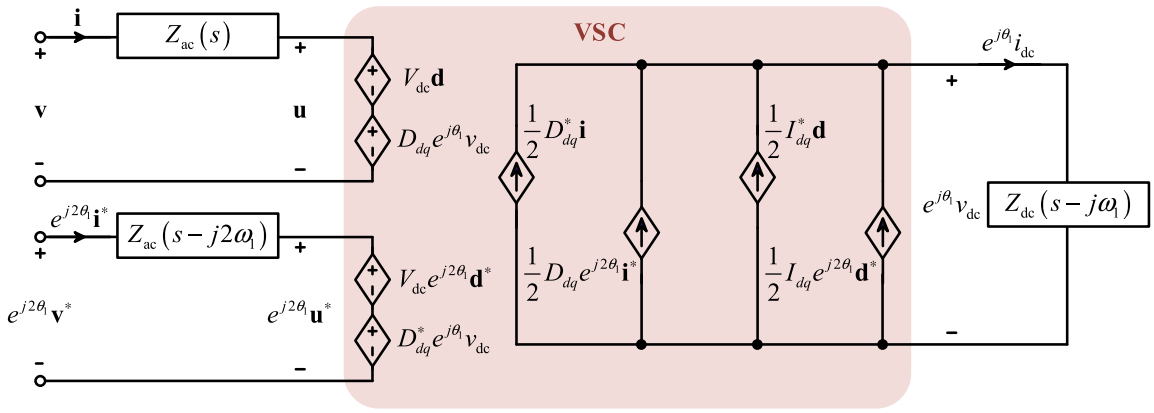

Fig. 2. Stationary-frame three-port small-signal circuit model for the VSC power stage.

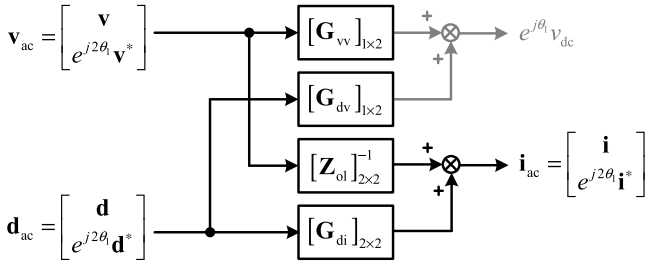

Fig. 3. Open-loop small-signal model for the VSC power stage.

$$[\mathbf{G}_{vv}]_{1\times2}=\frac{\frac{Z_{dc}(s-j\omega_1)}{2}\begin{bmatrix}D_{dq}^* & D_{dq}\end{bmatrix}\mathbf{Z}_{ac}^{-1}}{1+\frac{Z_{dc}(s-j\omega_1)}{2}\begin{bmatrix}D_{dq}^* & D_{dq}\end{bmatrix}\mathbf{Z}_{ac}^{-1}\begin{bmatrix}D_{dq}\\ D_{dq}^*\end{bmatrix}} \tag{17}$$

$$[\mathbf{G}_{dv}]_{1\times2}=\frac{\frac{Z_{dc}(s-j\omega_1)}{2}\left(\begin{bmatrix}I_{dq}^* & I_{dq}\end{bmatrix}-V_{dc}\begin{bmatrix}D_{dq}^* & D_{dq}\end{bmatrix}\mathbf{Z}_{ac}^{-1}\right)}{1+\frac{Z_{dc}(s-j\omega_1)}{2}\begin{bmatrix}D_{dq}^* & D_{dq}\end{bmatrix}\mathbf{Z}_{ac}^{-1}\begin{bmatrix}D_{dq}\\ D_{dq}^*\end{bmatrix}}. \tag{18}$$

It is noted that the $\mathbf{G}_{vv}$ and $\mathbf{G}_{dv}$ are both one-by-two matrices that map the relationships from ac-side signals to dc-side signal, while $\mathbf{Z}_{ol}$ and $\mathbf{G}_{di}$ are both two-by-two matrices that map the relationships between ac-side signals.

It is seen from Fig. 3 that there are actually dual complex-valued voltage inputs on the ac side, i.e., $\mathbf{v}$ and $e^{j2\theta_1}\mathbf{v}^*$, which is defined as the vector $\mathbf{v}_{ac}$. All the ac-side signals, i.e., $\mathbf{i}_{ac}$, $\mathbf{d}_{ac}$, and $\mathbf{u}_{ac}$ should all comply with this form.

As for the dc-side response, the output signal is $e^{j\theta_1}v_{dc}$, which is a complex scalar. There is only a single output signal on the dc side, whose signal flow is marked in gray shown in Fig. 3 to be distinguished from the dual inputs on the ac side.

It is noted that, the exponential operators, i.e., $e^{j2\theta_1}$ and $e^{j\theta_1}$, representing the time-periodic trajectory, are the origins of the frequency-coupling and phase-dependent dynamics for VSCs, wherein the $2\omega_1 t$ and $\omega_1 t$ indicate the coupling dynamics between two different frequency components, while the initial phases $2\varphi_1$ and φ_1 imply the phase dependence of the frequency-coupling transfer functions. Here these operators are intentionally combined with the input and output signals, instead of transfer functions, in the modeling, such that the derived transfer matrices can be treated as LTI and analyzed with the classical frequency-domain tools, e.g., the Bode diagrams and the generalized Nyquist stability criterion [20]. With the general form of the input and output signals at the ac and dc sides, the control dynamics of VSCs can be easily fit into the model.

C. DVC and PLL

For the system shown in Fig. 1, the VSC adopts two asymmetric control loops in the dq-frame, i.e., the DVC and the PLL. Here, the asymmetric control loop means that the control dynamics in d- and q-axes are different or the coupling control dynamics between d- and q-axes are not negated [12].

The DVC merely regulates the dc-link voltage and provides the d-axis current reference, i.e., $i_{d\text{ref}}$, and it thus results in the asymmetric control dynamic in the dq-frame. Defining $G_{DVC}(s)$ as the transfer function for the DVC, i.e., $G_{DVC}(s)=K_{PDVC}+(K_{IDVC}/s)$, in time domain, there exists

$$i_{d\text{ref}}=-G_{DVC}(p)v_{dc}. \tag{19}$$

Then, the small-signal $\mathbf{i}_{dq\text{ref}}$ is obtained as

$$\hat{\mathbf{i}}_{dq\text{ref}}=\hat{i}_{d\text{ref}}+j0=-G_{DVC}(p)\hat{v}_{dc}. \tag{20}$$

The PLL regulates the q-axis voltage to generate the phase of the input voltage, whose small-signal model is denoted by

$$\hat{\theta}=G_{PLL}(p)\hat{v}_q=G_{PLL}(p)\frac{e^{-j\theta_1}\hat{\mathbf{v}}-e^{j\theta_1}\hat{\mathbf{v}}^*}{2j} \tag{21}$$

where $G_{PLL}(s)=(K_{PPLL}s+K_{IPLL})/(s^2+K_{PPLL}V_d s+K_{IPLL}V_d)$ is the closed-loop transfer function of the PLL [11]. It is seen from (21) that the PLL only controls the q-axis voltage, which also results in asymmetric control dynamic in the dq-frame, thus the modeling with complex vectors cannot be simply analyzed in the single-input single-output (SISO) form, and the dynamic couplings between the two voltage inputs ($\mathbf{v}$ and $e^{j2\theta_1}\mathbf{v}^*$) should be considered [20].

The inverse Park transformation is applied to generate the current reference in the $\alpha\beta$-frame, such that

$$\mathbf{i}_{\text{ref}}=e^{j\theta}\mathbf{i}_{dq\text{ref}}=e^{j\theta_1}(1+j\hat{\theta})\mathbf{i}_{dq\text{ref}} \tag{22}$$

whose small-signal model can be represented as

$$\hat{\mathbf{i}}_{\text{ref}} = e^{j\theta_1}\hat{\mathbf{i}}_{dq\text{ref}} + jI_{dq\text{ref}}e^{j\theta_1}\hat{\theta}. \tag{23}$$

It can be seen from (23) that the dynamic of $\mathbf{i}_{\text{ref}}$ originates from both $\mathbf{i}_{dq\text{ref}}$ and θ, i.e., from both the DVC and the PLL.

Combining (20), (21), and (23), it can be derived that

$$\begin{aligned}\hat{\mathbf{i}}_{\text{ref}} = &-G_{\text{DVC}}(p-j\omega_1)e^{j\theta_1}\hat{v}_{\text{dc}} \\ &+\frac{I_{dq\text{ref}}}{2}G_{\text{PLL}}(p-j\omega_1)\hat{\mathbf{v}} - \frac{I_{dq\text{ref}}}{2} \\ &\times G_{\text{PLL}}(p-j\omega_1)e^{j2\theta_1}\hat{\mathbf{v}}^*.\end{aligned} \tag{24}$$

Similarly, applying the complex conjugate and the angle rotation successively to (24) yields

$$\begin{aligned}e^{j2\theta_1}\hat{\mathbf{i}}^*_{\text{ref}} = &-G_{\text{DVC}}(p-j\omega_1)e^{j\theta_1}\hat{v}_{\text{dc}} \\ &+\frac{I^*_{dq\text{ref}}}{2}G_{\text{PLL}}(p-j\omega_1)e^{j2\theta_1}\mathbf{v}^* - \frac{I^*_{dq\text{ref}}}{2} \\ &\times G_{\text{PLL}}(p-j\omega_1)\mathbf{v}.\end{aligned} \tag{25}$$

Then $\mathbf{Y}_{\text{DVC}}(s)$ and $\mathbf{Y}_{\text{PLL}}(s)$, which are defined as two admittance transfer matrices from the dc-side voltage and the ac-side voltage to the current reference, respectively, can be derived by substituting p with s in the following equation:

$$\begin{aligned}&\begin{bmatrix}\hat{\mathbf{i}}_{\text{ref}} \\ e^{j2\theta_1}\hat{\mathbf{i}}^*_{\text{ref}}\end{bmatrix} \\ &= -\underbrace{\begin{bmatrix}G_{\text{DVC}}(p-j\omega_1) \\ G_{\text{DVC}}(p-j\omega_1)\end{bmatrix}}_{[\mathbf{Y}_{\text{DVC}}(p)]_{2\times1}}e^{j\theta_1}\hat{v}_{\text{dc}} \\ &+\underbrace{\begin{bmatrix}\frac{I_{dq\text{ref}}}{2}G_{\text{PLL}}(p-j\omega_1) & -\frac{I_{dq\text{ref}}}{2}G_{\text{PLL}}(p-j\omega_1) \\ -\frac{I^*_{dq\text{ref}}}{2}G_{\text{PLL}}(p-j\omega_1) & \frac{I^*_{dq\text{ref}}}{2}G_{\text{PLL}}(p-j\omega_1)\end{bmatrix}}_{[\mathbf{Y}_{\text{PLL}}(p)]_{2\times2}} \\ &\times\begin{bmatrix}\mathbf{v} \\ e^{j2\theta_1}\mathbf{v}^*\end{bmatrix}\end{aligned} \tag{26}$$

D. CC and Time Delay

The VSC system also consists of symmetric control loops, such as the CC and the time delay. The CC is implemented in the $\alpha\beta$-frame with the PR regulator. There are no cross-coupling control terms between the α- and β-axes and the CC transfer functions are identical on both axes, thus the model can be represented in the complex space with a SISO complex transfer function [12] as

$$\mathbf{y} = \mathbf{G}_{\text{i}}(p)\mathbf{x} = (G_{\text{i}}(p) + j0)\mathbf{x} \tag{27}$$

where $\mathbf{x} = x_\alpha + jx_\beta$ denotes the input signal of the CC, and $\mathbf{y} = y_\alpha + jy_\beta$ denotes the output signal. $G_{\text{i}}(s) = (K_{\text{PI}} + (K_{\text{RI}}s)/(s^2+\omega_1^2))/(V_{\text{dc}})$ is the transfer function of the CC in the α- or β-frame, and $j0$ denotes the zero coupling control terms between the α- and β-axes. Similarly, with the complex conjugate and the angle rotation, it is derived that

$$e^{j2\theta_1}\mathbf{y}^* = \mathbf{G}^*_{\text{i}}(p-j2\omega_1)e^{j2\theta_1}\mathbf{x}^*. \tag{28}$$

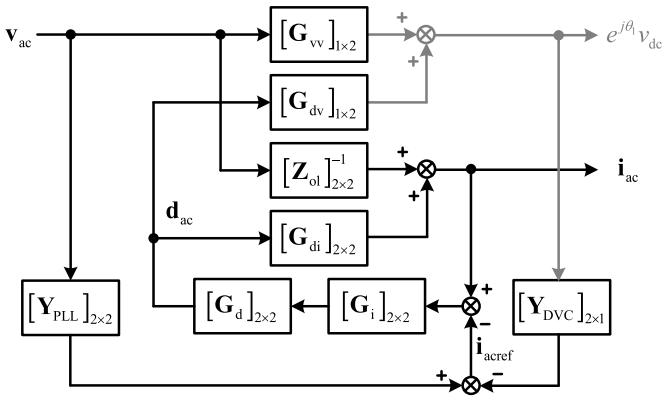

Fig. 4. Closed-loop small-signal model for the VSC.

Consequently, the CC in the $\alpha\beta$-frame can also be formulated with the general forms of ac-side signals. According to (27) and (28), the resultant transfer matrix is given by

$$[\mathbf{G}_{\text{i}}]_{2\times2} = \begin{bmatrix}\mathbf{G}_{\text{i}}(s) & \\ & \mathbf{G}^*_{\text{i}}(s-j2\omega_1)\end{bmatrix} = \begin{bmatrix}\text{G}_{\text{i}}(s) & \\ & \text{G}_{\text{i}}(s-j2\omega_1)\end{bmatrix} \tag{29}$$

where the off-diagonal elements are zero, which indicates that no frequency couplings are involved with the CC. It is noted that the form of (29) is general for any linear system in the $\alpha\beta$-frame, including control systems and balanced ac linear circuits.

Similarly, the time delay represented by the linear transfer function of $G_{\text{d}}(s) = e^{-sT_{\text{d}}} = e^{-1.5sT_{\text{s}}}$ can be formulated with the same form as (29). Then, the CC and the time delay can be integrated into the three-port small-signal model of the VSC.

E. Closed-Loop Small-Signal Model of VSC

Fig. 4 shows the closed-loop small-signal model of the VSC with all the control loops included. The black arrows denote the signal flows on the ac side and the gray arrows represent the signal flows on the dc side. Thus, the closed-loop complex transfer matrix from $\mathbf{v}_{\text{ac}}$ to $\mathbf{i}_{\text{ac}}$, i.e., the converter ac-side admittance $\mathbf{Y}_{\text{accl}}$, can be derived as (30), where $\mathbf{I}$ is a two-by-two identity matrix. The closed-loop complex transfer matrix from $\mathbf{v}_{\text{ac}}$ to $e^{j\theta_1}v_{\text{dc}}$, i.e., $\mathbf{G}_{\text{vvcl}}$, is derived as (31), which is a one-by-two matrix.

$$\begin{aligned}&[\mathbf{Y}_{\text{accl}}]_{2\times2} \\ &= \frac{\mathbf{i}_{\text{ac}}}{\mathbf{v}_{\text{ac}}} = [\mathbf{I} - \mathbf{G}_{\text{di}}(\mathbf{I} - \mathbf{G}_{\text{d}}\mathbf{G}_{\text{i}}\mathbf{Y}_{\text{DVC}}\mathbf{G}_{\text{dv}})^{-1}\mathbf{G}_{\text{d}}\mathbf{G}_{\text{i}}]^{-1} \\ &\quad\times\left[\mathbf{Z}^{-1}_{\text{ol}} - \mathbf{G}_{\text{di}}(\mathbf{I} - \mathbf{G}_{\text{d}}\mathbf{G}_{\text{i}}\mathbf{Y}_{\text{DVC}}\mathbf{G}_{\text{dv}})^{-1}\mathbf{G}_{\text{d}}\mathbf{G}_{\text{i}}\right. \\ &\qquad\left.\times(\mathbf{Y}_{\text{PLL}} - \mathbf{Y}_{\text{DVC}}\mathbf{G}_{\text{vv}})\right]\end{aligned} \tag{30}$$

$$\begin{aligned}&[\mathbf{G}_{\text{vvcl}}]_{1\times2} \\ &= \frac{e^{j\theta_1}v_{\text{dc}}}{\mathbf{v}_{\text{ac}}} = [1 - \mathbf{G}_{\text{dv}}(\mathbf{I} - \mathbf{G}_{\text{d}}\mathbf{G}_{\text{i}}\mathbf{G}_{\text{di}})^{-1}\mathbf{G}_{\text{d}}\mathbf{G}_{\text{i}}\mathbf{Y}_{\text{DVC}}]^{-1} \\ &\quad\times[\mathbf{G}_{\text{vv}} - \mathbf{G}_{\text{dv}}(\mathbf{I} - \mathbf{G}_{\text{d}}\mathbf{G}_{\text{i}}\mathbf{G}_{\text{di}})^{-1}\mathbf{G}_{\text{d}}\mathbf{G}_{\text{i}}(\mathbf{Y}_{\text{PLL}} - \mathbf{Z}^{-1}_{\text{ol}})]\end{aligned} \tag{31}$$

III. Physical Implications of Stationary-Frame Model

The physical implications of the stationary-frame ($\alpha\beta$-frame) complex-valued model are further discussed.

A. Phase-Dependent Effects

As aforementioned, the responses of the system are expressed by $\mathbf{v}_{ac}$, $\mathbf{i}_{ac}$, and $e^{j\theta_1}v_{dc}$, whose frequency-domain representations can be denoted by

$$\mathbf{v}_{ac}=\begin{bmatrix}\mathbf{v}\\ e^{j2\theta_1}\mathbf{v}^*\end{bmatrix}$$
$$\leftrightarrow \mathbf{V}_{ac}=\begin{bmatrix}\mathbf{V}(s)\\ e^{j2\varphi_1}\mathbf{V}^*(s-j2\omega_1)\end{bmatrix}$$
$$=\begin{bmatrix}V_\alpha(s)+jV_\beta(s)\\ e^{j2\varphi_1}(V_\alpha(s-j2\omega_1)-jV_\beta(s-j2\omega_1))\end{bmatrix} \quad (32)$$
$$\mathbf{i}_{ac}=\begin{bmatrix}\mathbf{i}\\ e^{j2\theta_1}\mathbf{i}^*\end{bmatrix}$$
$$\leftrightarrow \mathbf{I}_{ac}=\begin{bmatrix}\mathbf{I}(s)\\ e^{j2\varphi_1}\mathbf{I}^*(s-j2\omega_1)\end{bmatrix}$$
$$=\begin{bmatrix}I_\alpha(s)+jI_\beta(s)\\ e^{j2\varphi_1}(I_\alpha(s-j2\omega_1)-jI_\beta(s-j2\omega_1))\end{bmatrix} \quad (33)$$
$$e^{j\theta_1}v_{dc}\leftrightarrow e^{j\varphi_1}V_{dc}(s-j\omega_1). \quad (34)$$

Since s is represented by $j\omega$ in frequency domain, for $\mathbf{v}_{ac}$ and $\mathbf{i}_{ac}$, the first element implies the signal formulated by the first base vector at the frequency of ω, while the second element denotes the signal formulated by the second base vector at the frequency of $\omega-2\omega_1$ as well as a phase rotation related to $2\varphi_1$. Therefore, the frequency-shifted and phase-dependent responses will be generated on the ac side. Similarly, the dc-side response, $e^{j\theta_1}v_{dc}$, is also frequency shifted and phase dependent, where the frequency is shifted to $\omega-\omega_1$, and the phase is dependent on φ_1. It is important to note that differing from the dq-frame model, the phase dependence of the $\alpha\beta$-frame model is merely related to the initial phase φ_1, instead of the dynamic phase θ_1 [13].

The frequency-domain relationships from the input signal $\mathbf{v}_{ac}$ to the output signals $\mathbf{i}_{ac}$ and $e^{j\theta_1}v_{dc}$ can be represented as

$$\begin{bmatrix}\mathbf{I}(s)\\ e^{j2\varphi_1}\mathbf{I}^*(s-j2\omega_1)\end{bmatrix}=\underbrace{\begin{bmatrix}\mathbf{Y}_{ac11}(s) & \mathbf{Y}_{ac12}(s)\\ \mathbf{Y}_{ac21}(s) & \mathbf{Y}_{ac22}(s)\end{bmatrix}}_{\mathbf{Y}_{accl}}$$
$$\times\begin{bmatrix}\mathbf{V}(s)\\ e^{j2\varphi_1}\mathbf{V}^*(s-j2\omega_1)\end{bmatrix} \quad (35)$$
$$e^{j\varphi_1}V_{dc}(s-j\omega_1)=\underbrace{\begin{bmatrix}\mathbf{G}_{vv1}(s) & \mathbf{G}_{vv2}(s)\end{bmatrix}}_{\mathbf{G}_{vvcl}}$$
$$\times\begin{bmatrix}\mathbf{V}(s)\\ e^{j2\varphi_1}\mathbf{V}^*(s-j2\omega_1)\end{bmatrix} \quad (36)$$

where $\mathbf{Y}_{ac11}$, $\mathbf{Y}_{ac12}$, $\mathbf{Y}_{ac21}$, and $\mathbf{Y}_{ac22}$ are the four elements of the admittance matrix $\mathbf{Y}_{accl}$. $\mathbf{G}_{vv1}$ and $\mathbf{G}_{vv2}$ are the two elements of the transfer matrix $\mathbf{G}_{vvcl}$. It is worth mentioning that (35) and (36) can also be reformulated as

$$\begin{bmatrix}\mathbf{I}(s)\\ \mathbf{I}^*(s-j2\omega_1)\end{bmatrix}=\underbrace{\begin{bmatrix}\mathbf{Y}_{ac11}(s) & \mathbf{Y}_{ac12}(s)e^{j2\varphi_1}\\ \mathbf{Y}_{ac21}(s)e^{-j2\varphi_1} & \mathbf{Y}_{ac22}(s)\end{bmatrix}}_{\mathbf{Y}'_{accl}}$$
$$\times\begin{bmatrix}\mathbf{V}(s)\\ \mathbf{V}^*(s-j2\omega_1)\end{bmatrix} \quad (37)$$
$$V_{dc}(s-j\omega_1)=\underbrace{\begin{bmatrix}\mathbf{G}_{vv1}(s)e^{-j\varphi_1} & \mathbf{G}_{vv2}(s)e^{j\varphi_1}\end{bmatrix}}_{\mathbf{G}'_{vvcl}}$$
$$\times\begin{bmatrix}\mathbf{V}(s)\\ \mathbf{V}^*(s-j2\omega_1)\end{bmatrix} \quad (38)$$

where the phase-dependent terms are expressed within the transfer matrices instead of the input and output signals. It is clear that the phase dependence always comes with the frequency coupling transfer functions, i.e., the off-diagonal elements in the admittance matrix and both elements in the voltage transfer matrix. These phase-dependent terms are only related to the initial phase of the steady-state trajectory, which are constant. Therefore, each element of the transfer matrices is still characterized by LTI functions, which denotes the mapping relationship of the Fourier coefficients of the input and output signals at the corresponding frequency.

B. Physical Implications

Compared with the models in [13] and [20], the proposed model has direct physical implications, since it is derived directly based on the stationary-frame equivalent circuit shown in Fig. 2. To illustrate this, a comparison regarding different modeling procedures is shown in Fig. 5, where the main contributions of different modeling methods are highlighted in dashed boxes. It is seen that in both [13] and [20], the models are linearized around the time-invariant point based on the dq-frame equivalent circuit first, and then transformed to other frames by mathematical transformations. Therefore, the frequency coupling and phase dependence are explained from the mathematical basis. In contrast, the proposed model is directly linearized around the time-varying trajectory based on the $\alpha\beta$-frame equivalent circuit, without using any nonlinear transformations related to θ_1. Therefore, the frequency coupling and phase dependence can be characterized by the stationary-frame circuit model from a physical basis.

The $\alpha\beta$-frame complex-valued model directly maps the frequency couplings with the sequence components for three-phase systems, since the two base vectors denoted by $v_\alpha+jv_\beta$ and $v_\alpha-jv_\beta$ are mathematically equivalent to the time-dependent sequence components (u^+ and u^- introduced in [23]), except a scale factor of 1/2 for the magnitude-invariant form or $\sqrt{2}/2$ for the power-invariant form. However, the two base vectors do not essentially represent the positive-sequence component and negative-sequence component, respectively, since the sequence component is merely defined for a given positive frequency. For the $\alpha\beta$-frame model, the frequency of the second response is shifted to $\omega-2\omega_1$, which can be negative. That is to say, when $\omega>0$ and $\omega-2\omega_1<0$, both ac-side responses are positive-sequence components, and the

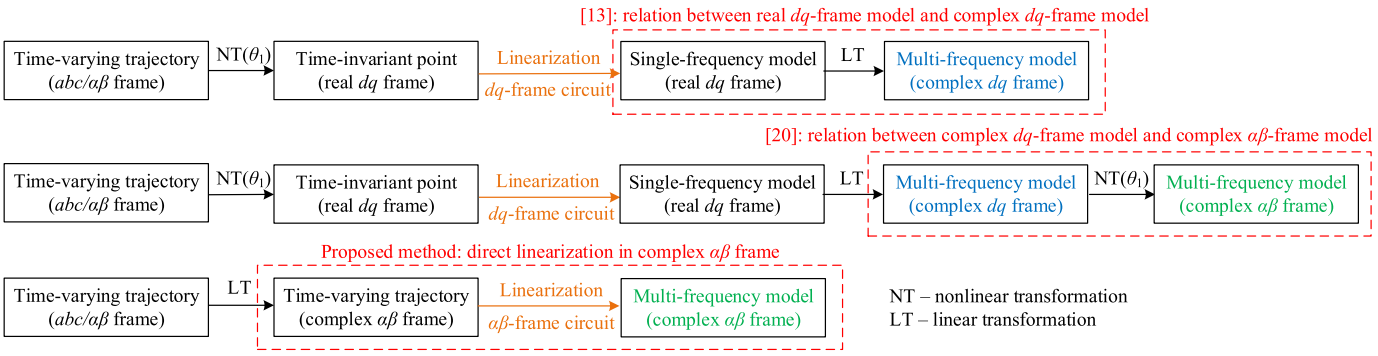

Fig. 5. Modeling procedures for VSCs by different methods.

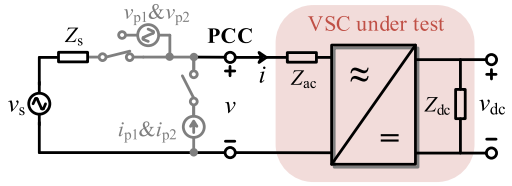

Fig. 6. Perturbation injection for frequency scan.

couplings between the positive-sequence component and the negative-sequence component do not exist.

IV. Frequency-Scan Approach

A frequency-scan approach to validating the stationary-frame complex-valued model of VSC is introduced in this section, where the frequency-coupling and phase-dependent properties are addressed. Then the advantages of the proposed frequency-scan approach over the existing approaches are summarized.

A. Measurement Method for VSC Frequency Response

A frequency-scan method for measuring the frequency response of the VSC is proposed, whose step-by-step procedure is shown in detail in Table I. Overall, there are three major steps as follows.

1) Perturbation Injection: To measure the six elements in the admittance and voltage transfer matrices, the system under test should be perturbed by at least two independent perturbations. The perturbation source can be either a voltage source (v_{p1} and v_{p2}) or a current source (i_{p1} and i_{p2}), as shown in Fig. 6, where the subscripts "1" and "2" indicate the first and second independent perturbations, respectively. It is important to guarantee that the steady-state voltage at point of common connection (PCC) maintains the same when the two perturbations are injected, respectively.

The perturbation frequency is scanned with ω changing ($\omega > 0$ rad/s). The two independent perturbations can be realized based on the definitions of the two base vectors. The first perturbation is determined by the first base vector only, i.e., $V_\alpha(s)+jV_\beta(s)$, and the second perturbation is determined by the second base vector only, i.e., $V_\alpha(s-j2\omega_1)-jV_\beta(s-j2\omega_1)$. The first perturbation can be realized by two sinusoidal signals at ω applied to α-axis and β-axis, respectively, with the β-axis initial phase lagging 90° of the α-axis initial phase. The second perturbation can be realized by two sinusoidal signals at $\omega-2\omega_1$ applied to α-axis and β-axis, respectively, with the β-axis initial phase leading 90° of the α-axis initial phase. The perturbation implementations are shown in Steps 1 and 4 in Table I.

TABLE I
Steps of the Frequency-Scan Method

Steps	Actions
Step 1	Inject the 1st perturbation at ω based on the 1st base vector: v_{p1} or i_{p1}
Step 2	Detect time-domain responses: $v_{\alpha1}$, $v_{\beta1}$, $i_{\alpha1}$, $i_{\beta1}$, v_{dc1}
Step 3	Calculate frequency-domain responses by DFT: $\begin{bmatrix}\mathbf{V}_1(\omega)\\ e^{j2\varphi_{11}}\mathbf{V}_1^*(\omega-2\omega_1)\end{bmatrix}=\begin{bmatrix}\mathcal{F}\{v_{\alpha1}(\omega)\}+j\mathcal{F}\{v_{\beta1}(\omega)\}\\ e^{j2\varphi_{11}}\left(\mathcal{F}\{v_{\alpha1}(\omega-2\omega_1)\}-j\mathcal{F}\{v_{\beta1}(\omega-2\omega_1)\}\right)\end{bmatrix}$ $\begin{bmatrix}\mathbf{I}_1(\omega)\\ e^{j2\varphi_{11}}\mathbf{I}_1^*(\omega-2\omega_1)\end{bmatrix}=\begin{bmatrix}\mathcal{F}\{i_{\alpha1}(\omega)\}+j\mathcal{F}\{i_{\beta1}(\omega)\}\\ e^{j2\varphi_{11}}\left(\mathcal{F}\{i_{\alpha1}(\omega-2\omega_1)\}-j\mathcal{F}\{i_{\beta1}(\omega-2\omega_1)\}\right)\end{bmatrix}$ $e^{j\varphi_{11}}V_{dc1}(\omega-\omega_1)=e^{j\varphi_{11}}\mathcal{F}\{v_{dc1}(\omega-\omega_1)\}$ where φ_{11} is the initial phase of the steady-state $v_{\alpha1}$, $\mathcal{F}\{x(\omega)\}$ means the Fourier coefficient of the signal x at ω
Step 4	Inject the 2nd perturbation at $\omega-2\omega_1$ based on the 2nd base vector: v_{p2} or i_{p2}
Step 5	Detect time-domain responses: $v_{\alpha2}$, $v_{\beta2}$, $i_{\alpha2}$, $i_{\beta2}$, v_{dc2}
Step 6	Calculate frequency-domain responses by DFT: $\begin{bmatrix}\mathbf{V}_2(\omega)\\ e^{j2\varphi_{12}}\mathbf{V}_2^*(\omega-2\omega_1)\end{bmatrix}=\begin{bmatrix}\mathcal{F}\{v_{\alpha2}(\omega)\}+j\mathcal{F}\{v_{\beta2}(\omega)\}\\ e^{j2\varphi_{12}}\left(\mathcal{F}\{v_{\alpha2}(\omega-2\omega_1)\}-j\mathcal{F}\{v_{\beta2}(\omega-2\omega_1)\}\right)\end{bmatrix}$ $\begin{bmatrix}\mathbf{I}_2(\omega)\\ e^{j2\varphi_{12}}\mathbf{I}_2^*(\omega-2\omega_1)\end{bmatrix}=\begin{bmatrix}\mathcal{F}\{i_{\alpha2}(\omega)\}+j\mathcal{F}\{i_{\beta2}(\omega)\}\\ e^{j2\varphi_{12}}\left(\mathcal{F}\{i_{\alpha2}(\omega-2\omega_1)\}-j\mathcal{F}\{i_{\beta2}(\omega-2\omega_1)\}\right)\end{bmatrix}$ $e^{j\varphi_{12}}V_{dc2}(\omega-\omega_1)=e^{j\varphi_{12}}\mathcal{F}\{v_{dc2}(\omega-\omega_1)\}$ where φ_{12} is the initial phase of the steady-state $v_{\alpha2}$, $\mathcal{F}\{x(\omega)\}$ means the Fourier coefficient of the signal x at ω
Step 7	Calculate the complex transfer matrices by (39) and (40): $\mathbf{Y}_{ac11}(\omega)$, $\mathbf{Y}_{ac12}(\omega)$, $\mathbf{Y}_{ac21}(\omega)$, $\mathbf{Y}_{ac22}(\omega)$ $\mathbf{G}_{vv1}(\omega)$, $\mathbf{G}_{vv2}(\omega)$

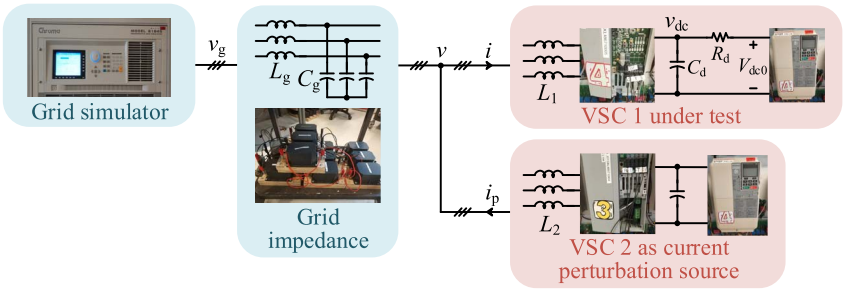

Fig. 7. Experimental setup for model validation.

2) Response Analysis: With the system perturbed by v_{pk} or i_{pk} ($k = 1$ or 2), there will be responses detected in the ac input voltage (v_k), the ac input current (i_k), and the dc voltage (v_{dck}), based on which the $\alpha\beta$-frame voltages ($v_{\alpha k}$ and $v_{\beta k}$) and currents ($i_{\alpha k}$ and $i_{\beta k}$) can be obtained, as shown in Steps 2 and 5. Through the discrete Fourier transform (DFT), the frequency-domain responses of the voltages and currents can be calculated by the equations shown in Steps 3 and 6. It can be seen that the dual ac-side responses are calculated with the Fourier coefficients of different frequency components based on the base vector definitions, indicating the frequency coupling effects.

In addition, the phase dependence of the initial phase (φ_{1k}) is also considered in the analysis. However, the initial phase is merely a static value, which can be easily analyzed by DFT analysis. This makes the $\alpha\beta$-frame model validation much simpler than the dq-frame model validation since no PLL is needed to capture the dynamic phase of the steady-state input voltage for Park transformation. It is important to note that for each time when the perturbation is injected, the initial phases of the steady-state input voltage can be different, i.e., φ_{11} and φ_{12}. Thus, they are calculated with the Fourier coefficients of the voltages and currents to validate $\mathbf{Y}_{\text{accl}}$ and $\mathbf{G}_{\text{vvcl}}$, and the different initial phases under different perturbations do not affect the calculation of the complex transfer matrices.

3) Calculation of Complex Transfer Matrix: Given the frequency responses of the voltages and currents under two perturbations, the frequency responses of the complex transfer matrices can be solved by (39) and (40), as shown in Step 7. Each element of the transfer matrices is an LTI transfer function expressed in the frequency domain.

$$\begin{bmatrix} \mathbf{Y}_{\text{ac11}}(\omega) & \mathbf{Y}_{\text{ac12}}(\omega) \\ \mathbf{Y}_{\text{ac21}}(\omega) & \mathbf{Y}_{\text{ac22}}(\omega) \end{bmatrix} = \begin{bmatrix} \mathbf{I}_1(\omega) & \mathbf{I}_2(\omega) \\ e^{j2\varphi_{11}}\mathbf{I}_1^*(\omega-2\omega_1) & e^{j2\varphi_{12}}\mathbf{I}_2^*(\omega-2\omega_1) \end{bmatrix} \times \begin{bmatrix} \mathbf{V}_1(\omega) & \mathbf{V}_2(\omega) \\ e^{j2\varphi_{11}}\mathbf{V}_1^*(\omega-2\omega_1) & e^{j2\varphi_{12}}\mathbf{V}_2^*(\omega-2\omega_1) \end{bmatrix}^{-1} \quad (39)$$

$$\begin{bmatrix} \mathbf{G}_{\text{vv1}}(\omega) & \mathbf{G}_{\text{vv2}}(\omega) \end{bmatrix} = \begin{bmatrix} e^{j\varphi_{11}}V_{\text{dc1}}(\omega-\omega_1) & e^{j\varphi_{12}}V_{\text{dc2}}(\omega-\omega_1) \end{bmatrix} \times \begin{bmatrix} \mathbf{V}_1(\omega) & \mathbf{V}_2(\omega) \\ e^{j2\varphi_{11}}\mathbf{V}_1^*(\omega-2\omega_1) & e^{j2\varphi_{12}}\mathbf{V}_2^*(\omega-2\omega_1) \end{bmatrix}^{-1} \quad (40)$$

TABLE II
FEATURES OF DIFFERENT FREQUENCY-SCAN APPROACHES

References	Model Frame	Frequency coupling	Phase dependence
[15]	Real dq frame	Not addressed	Not addressed
[13]	Complex dq frame	Indirectly addressed	Addressed (θ_1)
[22]	Complex $\alpha\beta$ frame	Directly addressed	Partially addressed (the off-diagonal elements cannot be verified)
Proposed approach	Complex $\alpha\beta$ frame	Directly addressed	Addressed (φ_1)

It is noted that the complex transfer matrices can be directly calculated by two responses under independent perturbations, thus the frequency scan method does not require any prior knowledge of the source impedance or test impedance, e.g., Z_{test} used in [22].

B. Advantages of the Proposed Frequency-Scan Approach

The proposed frequency-scan approach is developed for frequency-response validations of the $\alpha\beta$-frame complex-valued model, which can also be utilized to measure any other transfer function matrices of interest. Its properties are compared with other existing frequency-scan approaches, as shown in Table II.

It is found that differing from the dq-frame models, the $\alpha\beta$-frame complex-valued model can directly address the frequency couplings in the stationary frame without using the Park transformations, and therefore, there is no need to use a PLL to capture the dynamic information of $\theta_1 = \omega_1 t + \varphi_1$, which simplifies the model validation.

For the frequency-scan approach also developed for the $\alpha\beta$-frame complex-valued model in [22], the phase dependence is only partially addressed, and thus, the off-diagonal elements of the VSC impedance still cannot be measured. In contrast, the proposed frequency-scan approach is capable of measuring all elements of the VSC impedance, which makes it more convenient for validation and analysis of "black-box" systems.

V. VALIDATIONS AND DISCUSSION

The nonlinear time-domain simulations and experiments are carried out to validate the proposed modeling method for VSCs. The simulation is performed on the switching model

TABLE III
SYSTEM AND CONTROL PARAMETERS

Parameter	Value	Parameter	Value
V_g	200 V	I_p	3 A
L_g (ESR)	11 mH (0.3 Ω)	L_1 (ESR)	2 mH (0.1 Ω)
C_g	21 μF	L_2 (ESR)	2 mH (0.1 Ω))
C_d	0.45 mF	R_d	11 Ω
V_{dc0}	650 V	V_{dc}	620 V (Case A), 680 V (Case B)
f_1	50 Hz	f_s (=f_{sw}) / T_s	10 kHz / 0.1 ms
K_{PI}	5 Ω	K_{RI}	800 Ω/s
K_{PPLL}	0.58 rad/(s·V)	K_{IPLL}	27.2 rad/(s^2·V)
K_{PDVC}	0.5 S	K_{IDVC}	20 S/s

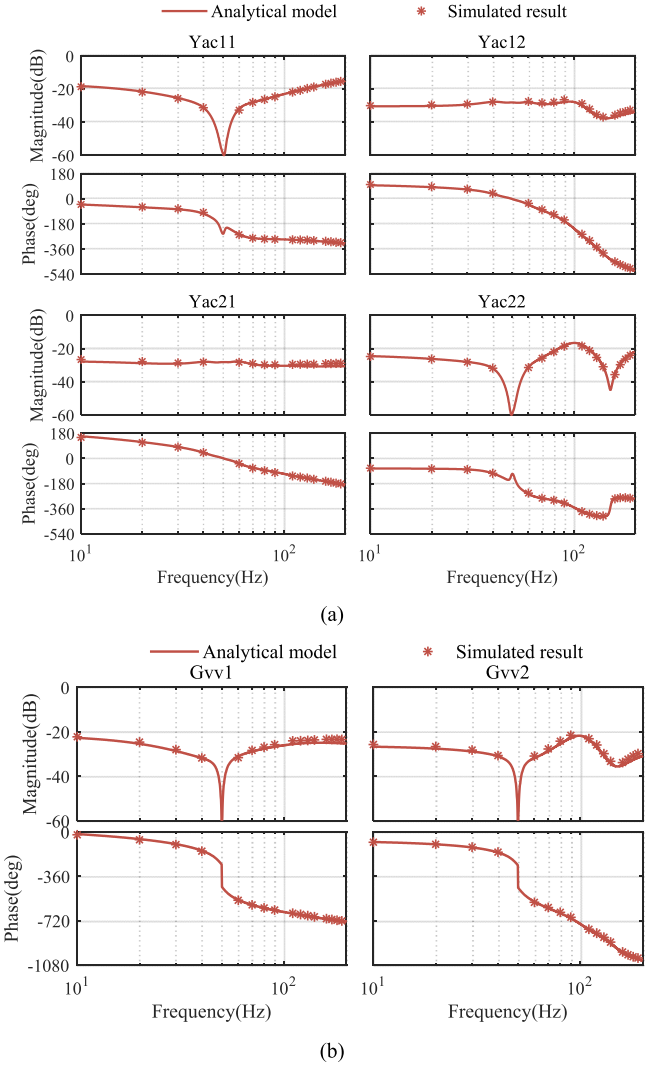

Fig. 8. Simulated results for Case A. (a) AC-side admittance. (b) AC–dc voltage transfer matrix

of VSC in the Simulink, which is set as the same as the experiment.

Fig. 7 shows the layout of the experimental setup used for validation, where the L-filtered converter VSC1 is connected to the grid simulator through a grid impedance. On the dc side, a dc voltage source V_{dc0} in series with R_d is used to generate a current source. The control is implemented as the same, as shown in Fig. 1. All the parameters are shown in Table III. The VSC2 is controlled as a current source to

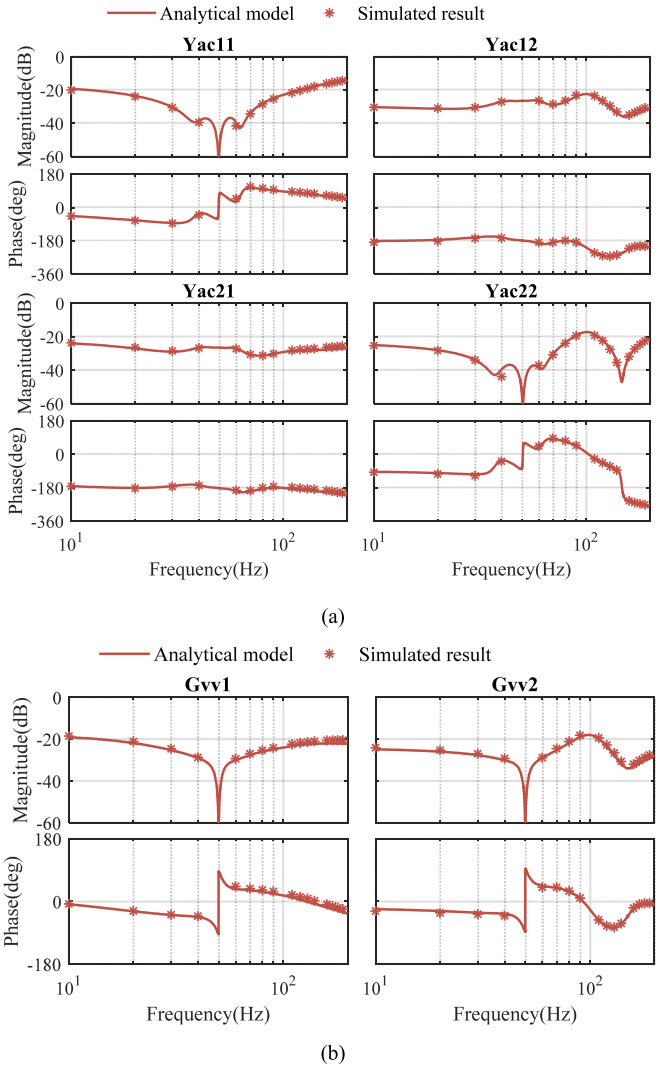

Fig. 9. Simulated results for Case B. (a) AC-side admittance. (b) AC–dc voltage transfer matrix.

inject perturbations into the system. The grid impedance is intentionally designed with large inductance to ensure that the needed current perturbation flows into the VSC1. It is noted that the grid impedance value influences the distribution of i_p between the VSC1 and the grid, thus the magnitude of the perturbation flowing into the VSC1 is important to the accuracy of the frequency scanned results [16].

A. Simulated Results

To validate the model, the VSC1 is simulated at different scenarios, i.e., inverter mode (Case A) and rectifier mode (Case B). Perturbations at different frequencies from 10 to 190 Hz are injected into the system by the VSC2. The frequency-scanned results are shown in Figs. 8 and 9. Fig. 8 shows the simulated results with Case A, and Fig. 9 shows the simulated results with Case B. The solid lines represent the analytical models of (30) and (31), where the steady-state values are calculated from the time-domain waveforms. The asterisks denote the simulated results obtained by the frequency-scan approach introduced in Section IV, which are in good alignment with the analytical models in both cases.

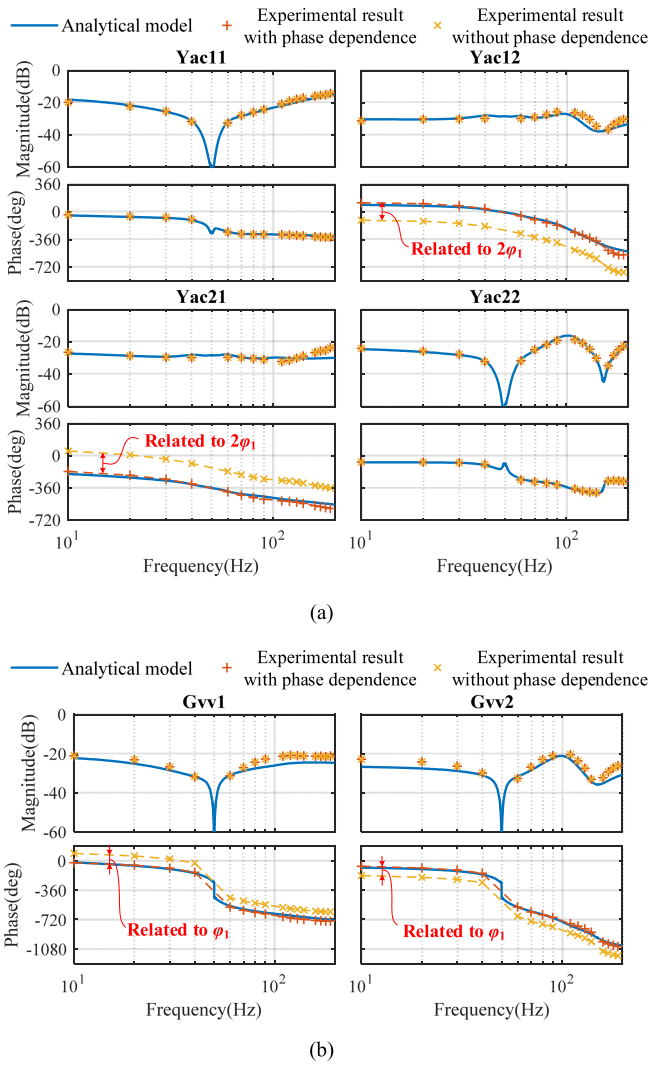

Fig. 10. Experimental results for Case A. (a) AC-side admittance. (b) AC–dc voltage transfer matrix.

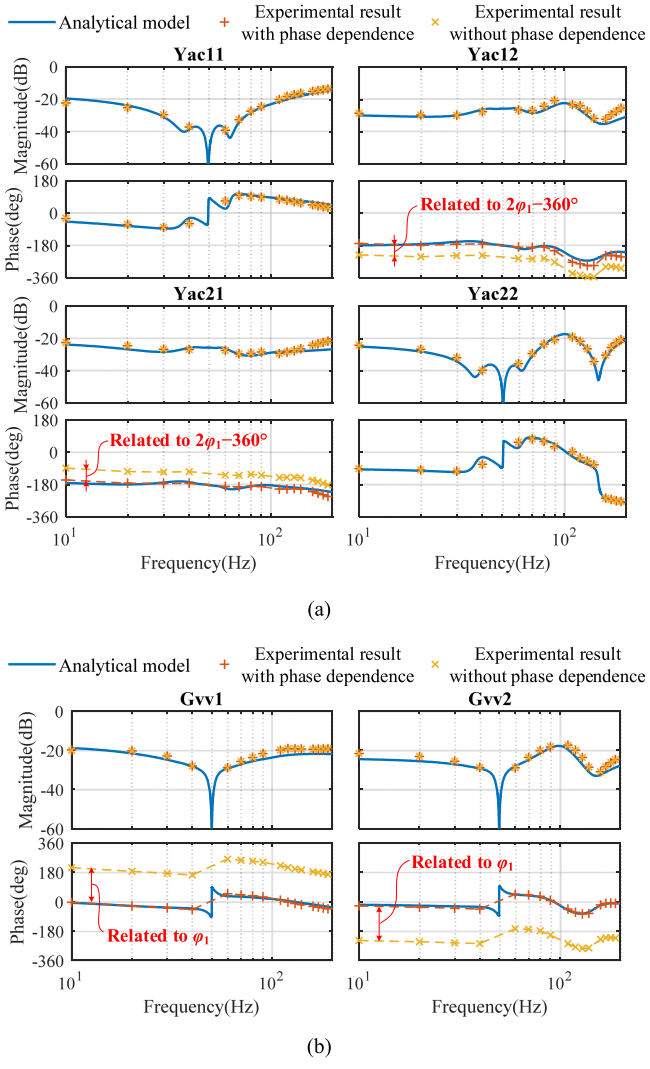

Fig. 11. Experimental results for Case B. (a) AC-side admittance. (b) AC–dc voltage transfer matrix.

It is thus verified that the proposed model is accurate for VSCs in different scenarios.

B. Experimental Results

Figs. 10 and 11 show the experimental results of the ac-side admittance and the ac–dc voltage-transfer matrix of the VSC1 for Cases A and B. The solid lines denote the analytical models, and the crosses denote the experimental results with or without phase dependence. It is seen that without considering the phase dependence, the experiment fails in an accurate estimation of the model in all the frequency-coupling terms. There are constant phase errors, which are impacted by the initial phase of the steady-state input voltage.

In contrast, the experimental results considering the phase dependence closely correlate with the analytical models. The slight differences in the off-diagonal elements of $\mathbf{Y}_{\text{ac}}$ (the frequency-coupling terms) are due to a few nonideal impact factors in the experimental setup. For clarify, the impacts of two particular factors, the inaccurate measurement sensors and the deadtime of VSC1, are analyzed in the following.

1) Impact of Inaccurate Measurement Sensors: The inaccuracy of the voltage and current sensors also has an impact on the experimental results. Fig. 12 compares the experimental results when the precalibration of measurement sensors is performed or not for Case A. It is clear that the precalibrated test leads to the closer correlation with the analytical model. The experimental results shown in Figs. 10 and 11 have been both refined with precalibration of the measurement sensors.

2) Deadtime Effect: The deadtime of 2 μs is adopted with VSC1 in experiments, whose impact on the impedance measurement is crosschecked by nonlinear time-domain simulations. Fig. 13 shows the simulated results with or without deadtime for Case A, comparing against the analytical model. It is obvious that the deadtime can lead to a similar mismatch in the off-diagonal elements of the admittance matrix in contrast to Fig. 10(a), especially in $\mathbf{Y}_{\text{ac21}}$. The mismatch is caused by the nonlinear effects of the deadtime on the impedance modeling and measurement [24].

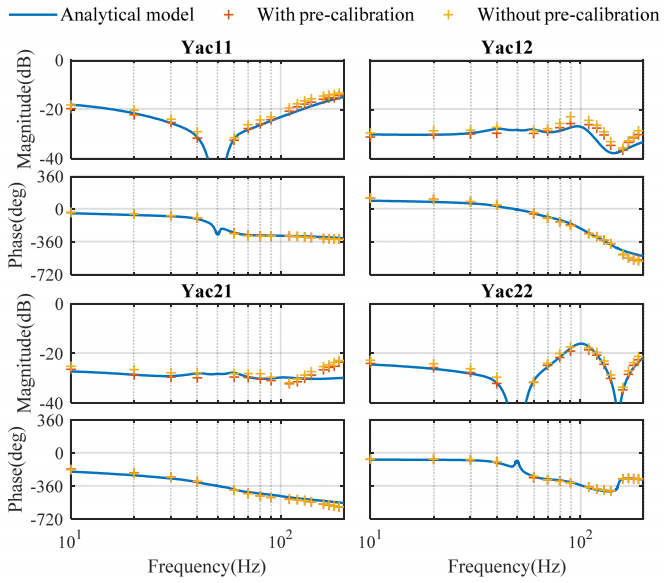

Fig. 12. Effect of the sensor precalibration on the admittance plot for Case A.

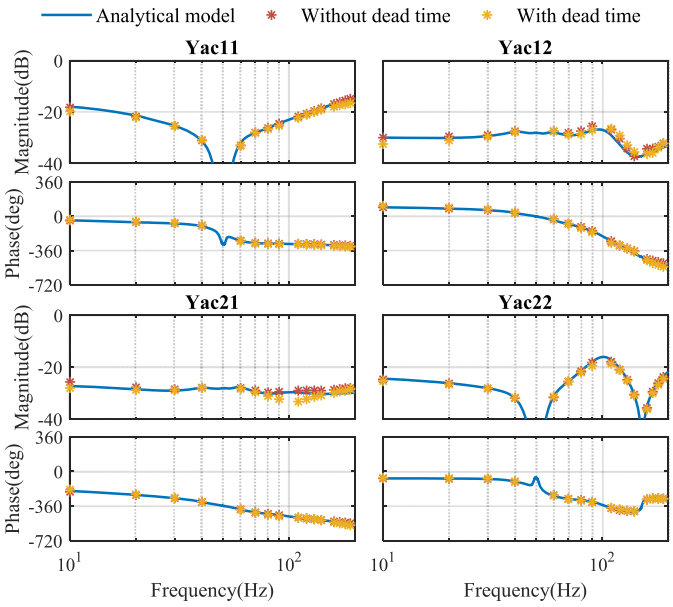

Fig. 13. Deadtime effect on the admittance plot for Case A.

C. Discussions

1) Phase Dependence Consideration: It is seen from Figs. 10 and 11 that without considering the phase dependence in measurement, there are constant phase shifts in the frequency-coupling terms that are related to the initial phase of the steady-state trajectory. The initial phase can be random in each measurement, therefore, as compared by Case A and Case B, the two initial phases are different, i.e., $\varphi_1 = 113.68°$ for Case A and $\varphi_1 = 212.59°$ for Case B. One can either consider the phase dependence with the analytical models, as indicated by (37) and (38), which are changing with φ_1, or consider the phase dependence with the frequency responses in measurement, as implied by (35) and (36) and addressed by the proposed frequency-scan approach. It is easier to implement the latter method for the VSC model validation, because the model remains independent of φ_1 for each measurement. If the former method is utilized for validation, a careful alignment of φ_1 for each perturbation injection in one measurement is required, which complicates the validation process.

On the other hand, if the impedance models are utilized for the system-level stability analysis with multiple converters, the phase dependence should be considered in the model by (37) and (38). In such cases, different converters are linearized around their own trajectories and, thus, have different phase-dependent terms. Combining these phase-dependent terms with the converter models can make the input–output signals independent of initial phases. These initial phases are static, which can be easily solved by the power flow calculation of the entire system or obtained by phasor measurement units.

2) Frequency Response Behaviors of the VSC: It can be seen from Figs. 8(a) and 9(a) that there is an anti-resonance at 50 Hz in $\mathbf{Y}_{\text{ac11}}$ and two anti-resonances at 50 and 150 Hz in $\mathbf{Y}_{\text{ac22}}$. Around the two frequencies, the magnitudes of $\mathbf{Y}_{\text{ac11}}$ and $\mathbf{Y}_{\text{ac22}}$ are much lower than those of $\mathbf{Y}_{\text{ac12}}$ and $\mathbf{Y}_{\text{ac21}}$, which implies that the frequency coupling effects are dominant around 50 and 150 Hz. This also explains why the frequency scan is implemented from 10 to 190 Hz in the validation. It is important to note that the two anti-resonances in $\mathbf{Y}_{\text{ac22}}$ are caused by the effect of the current-loop PR regulator on both positive- and negative-sequence components of 50 Hz. In addition, it can be found that the admittances shape differently around the fundamental frequency for the inverter mode and rectifier mode, which have different implications on the low-frequency stability as studied in [25].

For the ac–dc voltage-transfer matrix shown in Figs. 8(b) and 9(b), both elements involve the frequency-coupling effects. It can be found that the magnitudes of $\mathbf{G}_{\text{vv1}}$ and $\mathbf{G}_{\text{vv2}}$ are both very low, which means that the ac-side dynamics almost do not affect the dc-side dynamics. Similarly, two anti-resonances can be found in $\mathbf{G}_{\text{vv2}}$, which are also caused by the control effects of the current-loop PR regulator.

VI. Conclusion

In this article, a stationary-frame, frequency-domain modeling approach to three-phase converters has been developed step by step using complex vectors. A general stationary-frame three-port model for the VSC is put forward, considering the ac–dc interactions. With the complex-valued model, the frequency-coupling (i.e., $\omega-2\omega_1$ for ac side and $\omega-\omega_1$ for dc side) and the phase-dependent (i.e., $2\varphi_1$ for ac side and φ_1 for dc side) features of the VSC can be revealed explicitly. It is found that the phase dependence is related to the initial phase of the steady-state voltage and always comes with the frequency-coupling terms, which has a critical impact on the frequency-domain validation of the off-diagonal elements of the ac admittance matrix and the elements of the ac–dc voltage-transfer matrix of the VSC. Thus, considering the frequency-coupling terms and their phase dependence, a frequency scan method that is directly applied in the stationary frame has been further proposed. The frequency-scanned

results obtained from both nonlinear time-domain simulations and experimental tests closely match with the theoretical analysis. Therefore, the frequency-domain dynamics of three-phase converters can be directly characterized and validated in the stationary frame with the presented methods, which avoids the Park transformation and the PLL required in the conventional *dq*-frame modeling and frequency scan, and thus remarkably simplify the frequency-domain dynamic studies of the future converter-based power systems.

REFERENCES

[1] J. M. Undrill and T. E. Kostyniak, "Subsynchronous oscillations Part 1—Comprehensive system stability analysis," *IEEE Trans. Power App. Syst.*, vol. PAS-95, no. 4, pp. 1446–1455, Jul. 1976.

[2] J. Kwon, X. Wang, F. Blaabjerg, C. L. Bak, A. R. Wood, and N. R. Watson, "Linearized modeling methods of AC–DC converters for an accurate frequency response," *IEEE J. Emerg. Sel. Topics Power Electron.*, vol. 5, no. 4, pp. 1526–1541, Dec. 2017.

[3] A. R. Wood, D. J. Hume, and C. M. Osauskas, "Linear analysis of waveform distortion for HVDC and FACTS devices," in *Proc. 9th Int. Conf. Harmon. Qual. Power*, Orlando, FL, USA, Oct. 2000, pp. 967–972.

[4] E. V. Larsen, D. H. Baker, and J. C. McIver, "Low-order harmonic interactions on AC/DC systems," *IEEE Trans. Power Del.*, vol. 4, no. 1, pp. 493–501, Jan. 1989.

[5] M. Mohaddes, A. M. Gole, and S. Elez, "Steady state frequency response of STATCOM," *IEEE Trans. Power Del.*, vol. 16, no. 1, pp. 18–23, Jan. 2001.

[6] B. C. Smith, N. R. Waston, A. R. Wood, and J. Arrillaga, "Harmonic tensor linearisation of HVDC converters," *IEEE Trans. Power Del.*, vol. 13, no. 4, pp. 1244–1250, Oct. 1998.

[7] J. Kwon *et al.*, "Measurement of phase dependent impedance for 3-phase diode rectifier," in *Proc. 42nd Annu. Conf. IEEE Ind. Electron. Soc.*, Florence, Italy, Oct. 2016, pp. 7034–7039.

[8] X. Wang and F. Blaabjerg, "Harmonic stability in power electronic-based power systems: Concept, modeling, and analysis," *IEEE Trans. Smart Grid*, vol. 10, no. 3, pp. 2858–2870, May 2019.

[9] S. Hiti, D. Boroyevich, and C. Cuadros, "Small-signal modeling and control of three-phase PWM converters," in *Proc. IEEE Ind. Appl. Soc. Annu. Meeting*, Denver, CO, USA, Oct. 1994, pp. 1143–1150.

[10] L. Harnefors, M. Bongiorno, and S. Lundberg, "Input-admittance calculation and shaping for controlled voltage-source converters," *IEEE Trans. Ind. Electron.*, vol. 54, no. 6, pp. 3323–3334, Dec. 2007.

[11] B. Wen, D. Boroyevich, R. Burgos, P. Mattavelli, and Z. Shen, "Analysis of D-Q small-signal impedance of grid-tied inverters," *IEEE Trans. Power Electron.*, vol. 31, no. 1, pp. 675–687, Jan. 2016.

[12] L. Harnefors, "Modeling of three-phase dynamic systems using complex transfer functions and transfer matrices," *IEEE Trans. Ind. Electron.*, vol. 54, no. 4, pp. 2239–2248, Aug. 2007.

[13] A. Rygg, "Impedance-based methods for small-signal analysis of systems dominated by power electronics," Ph.D. dissertation, Dept. Eng. Cybern., Norwegian Univ. Sci. Technol., Trondheim, Norway, 2018.

[14] A. Rygg, M. Molinas, C. Zhang, and X. Cai, "A modified sequence-domain impedance definition and its equivalence to the dq-domain impedance definition for the stability analysis of AC power electronic systems," *IEEE J. Emerg. Sel. Topics Power Electron.*, vol. 4, no. 4, pp. 1383–1396, Dec. 2016.

[15] Z. Shen, "Online measurement of three-phase AC power system impedance in synchronous coordinates," Ph.D. dissertation, Dept. Elect. Eng., Virginia Polytech. Inst. State Univ., Blacksburg, VA, USA, 2012.

[16] H. Gong, D. Yang, and X. Wang, "Impact analysis and mitigation of synchronization dynamics for DQ impedance measurement," *IEEE Trans. Power Electron.*, vol. 34, no. 9, pp. 8797–8807, Sep. 2019.

[17] E. Mollerstedt and B. Bernhardsson, "Out of control because of harmonics-an analysis of the harmonic response of an inverter locomotive," *IEEE Control Syst. Mag.*, vol. 20, no. 4, pp. 70–81, Aug. 2000.

[18] V. Salis, A. Costabeber, S. M. Cox, F. Tardelli, and P. Zanchetta, "Experimental validation of harmonic impedance measurement and LTP Nyquist criterion for stability analysis in power converter networks," *IEEE Trans. Power Electron.*, vol. 34, no. 8, pp. 7972–7982, Aug. 2019.

[19] J. Sun and H. Liu, "Sequence impedance modeling of modular multilevel converters," *IEEE J. Emerg. Sel. Topics Power Electron.*, vol. 5, no. 4, pp. 1427–1443, Dec. 2017.

[20] X. Wang, L. Harnefors, and F. Blaabjerg, "Unified impedance model of grid-connected voltage-source converters," *IEEE Trans. Power Electron.*, vol. 33, no. 2, pp. 1775–1787, Feb. 2018.

[21] N. M. Wereley, "Analysis and control of linear periodically time varying systems," Ph.D. dissertation, Dept. Aeronaut. Astronaut., MIT, Cambridge, MA, USA, 1991.

[22] W. Ren and E. Larsen, "A refined frequency scan approach to sub-synchronous control interaction (SSCI) study of wind farms," *IEEE Trans. Power Syst.*, vol. 31, no. 5, pp. 3904–3912, Sep. 2016.

[23] G. C. Paap, "Symmetrical components in the time domain and their application to power network calculations," *IEEE Trans. Power Syst.*, vol. 15, no. 2, pp. 522–528, May 2000.

[24] M. Zhang, D. Yang, and X. Wang, "Accurate open-loop impedance model of single-phase voltage source inverter (VSI) considering the dead-time effects," in *Proc. 20th Workshop Control Modeling Power Electron. (COMPEL)*, Toronto, ON, Canada, Jun. 2019, pp. 1–5.

[25] D. Lu, X. Wang, and F. Blaabjerg, "Impedance-based analysis of DC-link voltage dynamics in voltage-source converters," *IEEE Trans. Power Electron.*, vol. 34, no. 4, pp. 3973–3985, Apr. 2019.

Yicheng Liao (Student Member, IEEE) received the B.S. degree in electrical engineering and its automation and the M.S. degree in electrical engineering from Southwest Jiaotong University, Chengdu, China, in 2015 and 2018, respectively. She is currently pursuing the Ph.D. degree in power electronics engineering from Aalborg University, Aalborg, Denmark.

She was a Visiting Student with Ecole Polytechnique and Inria, Paris, France, in July 2017. She has been a Research Assistant with the Department of Energy Technology, Aalborg University, since September 2018. Her research interests include the modeling, stability analysis, and control of power electronics-based power systems.

Xiongfei Wang (Senior Member, IEEE) received the B.S. degree in electrical engineering from Yanshan University, Qinhuangdao, China, in 2006, the M.S. degree in electrical engineering from the Harbin Institute of Technology, Harbin, China, in 2008, and the Ph.D. degree in energy technology from Aalborg University, Aalborg, Denmark, in 2013.

Since 2009, he has been with the Department of Energy Technology, Aalborg University, where he became an Assistant Professor in 2014, an Associate Professor in 2016, a Professor and Research Program Leader of electronic power grid (eGrid) in 2018, and the Director of Aalborg University - Huawei Energy Innovation Center in 2020. His current research interests include modeling and control of grid-interactive power converters, stability and power quality of converter-based power systems, and active and passive filters.

Dr. Wang was selected into Aalborg University Strategic Talent Management Program in 2016. He has received the six IEEE prize paper awards, the 2016 Outstanding Reviewer Award of the IEEE TRANSACTIONS ON POWER ELECTRONICS, the 2018 IEEE PELS Richard M. Bass Outstanding Young Power Electronics Engineer Award, the 2019 IEEE PELS Sustainable Energy Systems Technical Achievement Award, and the 2019 Highly Cited Researcher by Clarivate Analytics (former Thomson Reuters). He serves as a Member-at-Large for Administrative Committee of the IEEE Power Electronics Society from 2020 to 2022, and an Associate Editor for the IEEE TRANSACTIONS ON POWER ELECTRONICS, the IEEE TRANSACTIONS ON INDUSTRY APPLICATIONS, and the IEEE JOURNAL OF EMERGING AND SELECTED TOPICS IN POWER ELECTRONICS.